Journal of Electric Propulsion

RESEARCH Open Access

A theoretical thrust density limit for Hall thrusters

Jacob Simmonds[1,2*], Yevgeny Raitses[2†] and Andrei Smolyakov[3†]

†Yevgeny Raitses and Andrei Smolyakov contributed equally to this work.

*Correspondence: jacobbs@princeton.edu

[1] Mechanical and Aerospace Engineering, Princeton University, Princeton 08543, NJ, USA
[2] Plasma Sciences and Technology, Princeton Plasma Physics Laboratory, 100 Stellarator Road, Princeton 08544, NJ, USA
[3] Theoretical Plasma Physics, University of Saskatchewan, 116 Science Place, Saskatoon S7N 5E2, SK, Canada

Abstract

Hall Thrusters typically operate at thrust densities on the order of 10 N/m^2, which appear to be orders of magnitude below the thrust density limits suggested in previous literature. These limits have been considered here and each component of thrust density is analyzed to demonstrate the relative contribution to the total thrust density. Dependencies of the thrust density limits upon the thruster geometry, electron mobility, and the applied magnetic field are revealed and compared with experimental measurements of thrust density. This analysis reveals that with conventional applied magnetic field strengths, Hall thruster thrust density appears to be on the order of 1000 N/m^2. It is shown that this limit can be further increased through higher applied magnetic fields, applied voltage, and suppression of anomalous electron transport. This suggests Hall thrusters can be made much more compact and operated at higher power densities, given improvements to the thermal management and materials.

Keywords: Hall thruster, Thrust density, Magnetic pressure

Introduction

Hall Effect Thrusters (HET) are quickly maturing as a technology to become the most common form of electric propulsion in space [1]. Recent scientific missions such as PSYCHE now utilize a Hall thruster as the main propulsion unit for deep-space orbital transits and maneuvering [2], and large constellations of commercial satellites such as Starlink rely upon HET to maintain their orbits. These new developments are brought about by two converging factors in the space industry: the rise of higher power capabilities onboard satellites and the miniaturization of components. These two enabling developments call for thruster technologies that can provide high throughput at small physical scales. A quantitative measure of such a quantity is the thrust density of the thruster, which is simply the thrust generated divided by the front-facing area of the thruster. The interest and development of HET is in part due to their favorable thrust density compared to other forms of electric propulsion such as gridded ion thruster in the 100 W - 10 kW power range, as well as their favorable thrust-specific impulse ratio.

There remain several unanswered questions surrounding the potential limits of Hall thruster thrust density. These questions are driven by the potential benefits of operating at higher thrust densities, namely, if Hall thrusters are able to function with higher thrust

density, smaller thrusters could be used on spacecraft which would allow more volume and mass for payload or fuel. It was suggested previously [3] that that the maximum achievable thrust density in HET is limited by the magnetic pressure of the magnetic field (B) in the thruster: $B^2/2\mu_0$ [3]. This limit is typically orders of magnitude higher than the thrust density in currently operating thrusters (see Fig. 1). Various formulations of the thrust density limits are revisited here in an attempt to reveal several constraints and dependencies on Hall thruster parameters.

This article is organized as follows. In the Background section, an overview of previous literature on thrust density derivations is provided. In the Thrust density evaluation section, an expression for the thrust density is derived for HET. The thrust density is expanded into four distinct components related to distinct physical mechanisms, which are analyzed in the Magnetic pressure and tension section: magnetic pressure and tension, plasma resistivity, plasma pressure, and magnetic mirroring of electrons. The relative contributions of each of these components to thrust density is discussed and compared to experimental data in the Relative contributions section, the limit of thrust density is derived in the Thrust density limit section for a variety of electron transport models, and conclusions are discussed in the Conclusion section.

Background

The goal of any thruster system is to accelerate ions as the particles with a finite mass (compared to the negligible mass of electrons). At a very high level, it is useful to consider the total kinetic and electric potential energy of the ions: $E_i = m_i(V_z^2 + V_\theta^2 + V_r^2)/2 + q\phi$. Here, E_i is ion energy, m_i is ion mass, V_z, V_θ, and V_r are ion velocity in the axial azimuthal and radial direction, q is charge, and ϕ is potential energy. From this perspective, the thrust is associated with the axial ion energy due to the ion axial velocity, V_z. According to energy conservation, the axial ion energy can be directly converted from the electrostatic potential energy (via the axial electric field, E_z)

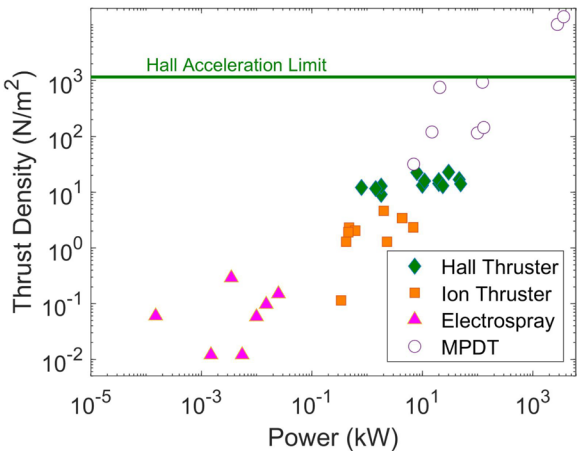

Fig. 1 Measured thrust densities versus power of several forms of electric propulsion. Area is total thruster area as defined by the channel diameter. The approximate Hall acceleration limit due to magnetic pressure is shown as a solid green line for a typical thruster magnetic field of 300 G, assuming Bohm diffusion as derived in Bohm diffusion section. Note that Hall thrusters are operating below this limit. Thrusters and references are shown in Appendix A

as it occurs /textcolorbluedirectly in electrostatic ion thrusters. Additional mechanisms are related to the conversion of the ion perpendicular energy into the energy of the axial motion ($\sim (V_\theta^2 + V_r^2) \rightarrow V_z^2$). Given that the static magnetic field does not change the energy of charged particles, only rotates the direction of the velocity vector, the energy must initially be gained by the electric field, particularly given ions are often unmagnetized in plasma thrusters, such as is the case for HET. The magnetic field is paramount however to create the conditions to sustain a large electric field through magnetized electrons (as in Hall thrusters), supply the perpendicular energy and convert the energy of the perpendicular motion (like rotation) into the axial energy (as in magnetoplasmadynamic thrusters: MPDTs).

The deposition of energy into the ion axial motion has to be considered together with the momentum balance, in particular, with the momentum exchange between ion and electron components. In a quasineutral plasma, this momentum exchange occurs via the electric field. Neglecting the electron inertia one can write

$$-en\left(\vec{E} + \vec{V}_e \times \vec{B}\right) - \vec{\nabla} P_e + \vec{R}_e = 0, \tag{1}$$

$$m_i\left(\vec{V}_i \cdot \vec{\nabla}\right)\vec{V}_i = en\left(\vec{E} + \vec{V}_i \times \vec{B}\right) + \vec{R}_i = 0. \tag{2}$$

Here e is electron charge, n is plasma density, $\vec{E}$ is the electric field, $\vec{V}_e$ is the electron velocity, $\vec{V}_i$ is ion velocity, $\vec{B}$ is the magnetic field, P_e is the electron pressure, and $\vec{R}_e$ and $\vec{R}_i$ are the electron and ion collision momentum terms. For simplicity we omit here the ion pressure compared to the ion kinetic energy of the directed motion. One can also consider the equivalent equation for the total ion+electron momentum in the form

$$m_i\left(\vec{V}_i \cdot \vec{\nabla}\right)\vec{V}_i = \vec{J} \times \vec{B} - \vec{\nabla} P_e + \left(\vec{R}_i + \vec{R}_e\right) = 0. \tag{3}$$

Where $\vec{J} = en(\vec{V}_i - \vec{V}_e)$ is the total current. Equations (1), (2), and (3) illustrate the duality of the acceleration mechanism in HET. Equation 2 shows that ions are accelerated by the electric field, hence the mechanism is electrostatic, while Eq. (3) show that the total momentum to the plasma (mostly residing in ions) is provided by the $J \times B$ force, which also applies to the magnetic system. Hence, it can be viewed as an electromagnetic acceleration given the thrust is applied to the magnets. Of course, both interpretations are correct and it is a matter of terminology [4, 5].

Based on the definition in Eq. (3), the force on the plasma $\vec{F}_{EM}$ can be estimated [3] based on the magnetic pressure from the electromagnetic force

$$\vec{F}_{EM} = \vec{J} \times \vec{B} \sim \nabla \frac{B^2}{2}. \tag{4}$$

The total magnetic pressure however provides a highly overestimated limit for the thrust density. As a matter of fact, the electromagnetic force consists of the magnetic pressure and curvature forces,

$$\vec{F}_{EM} = \vec{J} \times \vec{B} = -\frac{\nabla(B^2)}{2\mu_0} + \frac{\left(\vec{B} \cdot \vec{\nabla}\right)\vec{B}}{\mu_0}, \tag{5}$$

which cancel each other exactly for the vacuum magnetic field. The total input of the momentum based on Eq. (5) is finite only due to the deviation of the magnetic field from its vacuum value. This deviation is small for the Hall thruster but cannot be neglected when using this expression.

From Eq. (2) and neglecting the effects of the magnetic field on ions, one can see that the momentum input on ions is due to the axial electric field. For Hall thrusters, with predominantly radial magnetic fields, the axial electric field on the electrons is offset by the Lorentz force generated by the induced Hall current in the cross-fields in the channel. The axial electron stress force (pressure gradient and anisotropic stress tensor), as well as the friction force may also provide some contributions.

The generation of an electric field in a quasineutral plasma allows Hall thrusters to achieve thrust densities above that of gridded ion thrusters, which are limited by the space charge in the accelerator grid gaps (giving rise to the familiar Child-Langmuir law behavior) [6]. There have been some investigations into gridded ion thruster-Hall thruster hybrids, such as the NASA-173GT which was designed to achieve the high specific impulse of gridded ion thrusters while retaining a Hall acceleration stage [7], the Dual-Mode Hybrid Engine which essentially packs two thrusters together [8], and other designs which utilize the injection of negative ions to purports to achieve an increase in thrust density by neutralizing the space charge [9].

When the axial magnetic field is included B_z, such as in the magnetic nozzle (see Fig. 2) and cylindrical Hall thruster configurations [10], the radial electron pressure gradient affects the azimuthal motion and thus becomes a part of the total thrust [11, 12]. It is shown in these works that by neglecting electron-neutral collisions, which are assumed to be negligible for the magnetic nozzle thruster, the radial plasma pressure balances the azimuthal current $j_\theta \times B_z$ force. This assumption cannot be made for high thrust density HET, as electron-neutral collisions are both critical to maintaining current continuity and are shown in Magnetic pressure and tension section to be a limiting factor in the thrust density. The combined effects of the radial and axial magnetic field (in the nozzle

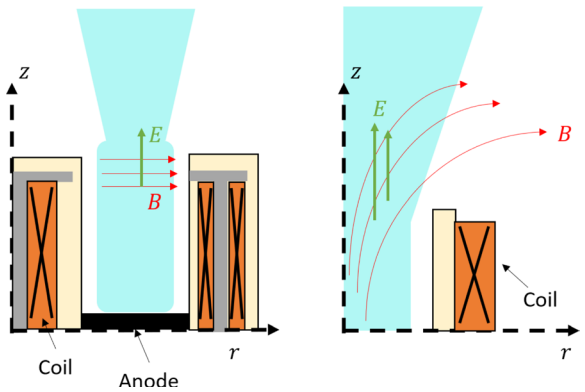

Fig. 2 Sketch of a Hall thruster (left) and magnetic nozzle (right) with corresponding cylindrical coordinate systems

configuration) allows the conversion of the plasma (ion) perpendicular momentum (mostly azimuthal) into the axial motion which is termed as an electromagnetic acceleration mechanism in [5, 13]. According to the terminology in [5, 13], the configurations with diverging magnetic field (magnetic nozzle) exhibit hybrid (electrostatic and electromagnetic) acceleration mechanisms.

In this manuscript, we estimate relative contributions of various contributions focusing on the geometry of the annular HET, where only the radial magnetic field is considered. The self-consistently generated magnetic field is considered in this derivation and the resulting inputs are evaluated and compared with some available experimental data.

Thrust density evaluation

In Hall thrusters, thrust is generated by the acceleration of ions across an electric field, which is generated in the plasma by the reduced mobility of electrons in an applied magnetic field. The thrust density can be related to this electric field by integrating the product of the charge e, the electron plasma density n_e and the axial component of the electric field E_z over the axial domain z_0 to z_f, and some front-facing area A, an expression which evolves from the electrostatic force:

$$T = \int^{A} \int_{z_o}^{z_f} e n_e E_z dz dA \,. \tag{6}$$

The area A in this expression is defined for practical purposes as the front-facing area of the thruster, which is simply the area within the outer diameter of the channel containing the plasma. This was done purely to compare between different thrusters, as it can be unclear which part of the area should be used when considering gridded ion thrusters, MPDTs, cylindrical Hall thrusters, etc. There is some rationale behind using only the channel area of the thruster, particularly as this is where much of the derived acceleration occurs, however this neglects the fact that there are instances where ions are accelerated outside of the channel, both in the center of the HET [14] as well as outside of the channel. The area bounded by the outer channel provides more of an engineering view of the thrust density as it relates to the size of the thruster itself, and removes the edge cases such as when a very narrow channel is used. The thrust density for the thruster, assuming uniformity over the cross-sectional area, is then simply

$$\mathcal{T} = \frac{T}{A} = \int_{z_o}^{z_f} e n_e E_z dz \,. \tag{7}$$

The electric field E can be solved by utilizing the steady-state electron fluid momentum balance equations. This is done under the assumption of electron momentum continuity, steady-state operation of the thruster, and negligible contribution of electron-electron and electron-ion collisions.

$$0 = -e n_e (\vec{E} + \vec{u} \times \vec{B}) - m_e n_e \nu_{en} \vec{u} - \vec{\nabla} \cdot \bar{\bar{P}} \,, \tag{8}$$

$$\vec{E} = -(\vec{u} \times \vec{B}) - \frac{m_e \nu_{en}}{e} \vec{u} - \frac{1}{e n_e} \vec{\nabla} \cdot \bar{\bar{P}} \,, \tag{9}$$

where u is the electron fluid velocity, B is the magnetic field, m_e is the mass of an electron, ν_{en} is the electron-neutral collision frequency, and $\bar{\bar{P}}$ is the electron plasma pressure tensor. If we at first define our coordinate system by the parallel and perpendicular components of the magnetic field, [15] we can expand the pressure term by the following:

$$E_{\parallel} = \frac{m_e \nu_{en}}{e} u_{\parallel} - \frac{1}{e n_e}\left(\nabla_{\parallel} P_{\parallel} - \left(\frac{P_{\parallel} - P_{\perp}}{B}\right)\nabla_{\parallel} B\right) \tag{10}$$

$$E_{\perp} = -(\vec{u} \times \vec{B})_{\perp} - \frac{m_e \nu_{en}}{e} u_{\perp} - \frac{1}{e n_e}(\nabla_{\perp} P_{\perp})\,. \tag{11}$$

To return to cylindrical coordinates for the purposes of calculating E_z for a thruster, we must take into account some angle α as shown in Fig. 3. The z component is simply the parallel and perpendicular of the previous equations scaled by the cosine and sine of α respectively:

$$\begin{aligned} E_z = &-(\vec{u} \times \vec{B})_z - \frac{m_e \nu_{en}}{e} u_z - \frac{1}{e n_e}\left(\nabla_z (P_{\parallel} \cos^2\alpha + P_{\perp} \sin^2\alpha)\right) \\ &- \frac{\cos^2\alpha}{e n_e}\left(\frac{P_{\perp} - P_{\parallel}}{B}\right)\nabla_z B\,. \end{aligned} \tag{12}$$

We will then convert the electron fluid velocities into current by the relation $\vec{j} = -e n_e \vec{u}$:

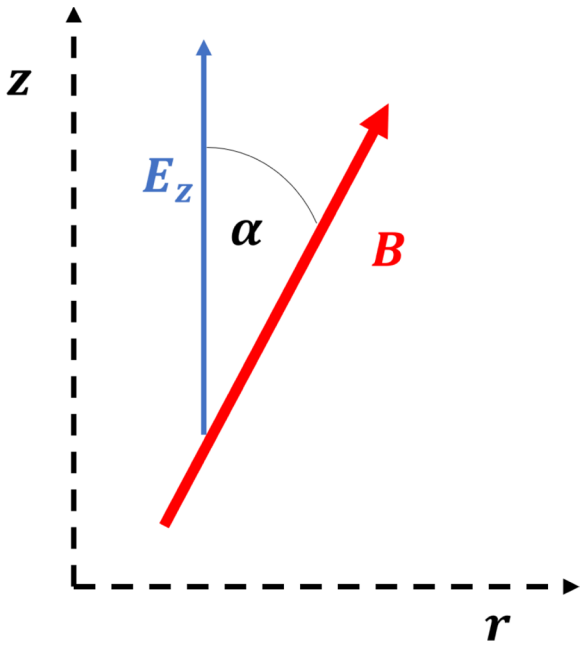

Fig. 3 Angle between magnetic field and axial electric field

$$E_z = \frac{1}{en_e}(\vec{j} \times \vec{B})_z + \frac{m_e \nu_{en}}{e^2 n_e} j_z - \frac{1}{en_e}\left(\nabla_z (P_\parallel \cos^2\alpha + P_\perp \sin^2\alpha)\right) - \frac{\cos^2\alpha}{en_e}\left(\frac{P_\perp - P_\parallel}{B}\right)\nabla_z B\,. \tag{13}$$

The electric field is then due to the sum of four components in Eq. (13): 1) magnetic pressure & tension, 2) axial resistivity pressure, 3) plasma pressure, and 4) magnetic mirror pressure. We will now solve each individually:

$$E_z = E_{z,1} + E_{z,2} + E_{z,3} + E_{z,4}\,. \tag{14}$$

Magnetic pressure and tension

The first component, which we will soon find is related to the magnetic pressure and tension, is

$$E_{z,1} = \frac{1}{en_e}(\vec{j} \times \vec{B})_z\,. \tag{15}$$

The electron current in the plasma is not known, however we are able to determine the maximum current possible before the induced magnetic field overwhelms the externally applied magnetic field. The current can be related to the curl of the magnetic field through Maxwell's equations:

$$\vec{j} = \frac{1}{\mu_0}\vec{\nabla} \times \vec{B}\,, \tag{16}$$

where μ_0 is the magnetic permeability of free space. Substituting Eq. (16) into Eq. (15):

$$E_{z,1} = \frac{1}{en_e}(\vec{j} \times \vec{B})_z = -\frac{1}{en_e}\left(\frac{\vec{\nabla}_\perp (B^2)}{2\mu_0} - \frac{B^2}{\mu_0}\frac{\hat{R}_B}{R_B}\right)_z\,, \tag{17}$$

where the first term on the right hand side (RHS) is the magnetic pressure in the system and the second term on the RHS is the magnetic tension, and $\hat{R}_B$ is the outward pointing vector of the radius of curvature of the magnetic field. For straight radial magnetic fields with no curvature or gradient, both the magnetic pressure and tension are zero, which is often the idealized assumption for the field formed in an annular HET channel. For magnetic fields with some finite curvature and field gradient, which is a typical case in Hall thrusters, if there is no current-induced magnetic field the pressure and tension balance each other such that they sum to zero. This continues to be the case for thrusters with strong axial fields, such as cylindrical Hall thrusters, [10] although the magnitude of both the magnetic pressure and tension terms tend to be higher due to the stronger gradients and curvature.

The limit of the magnetic pressure and tension term can be derived for the case of a simplified annular Hall thruster configuration. Consider an annular HET with a magnetic field which only has a radial component, such as shown in Fig. 4. In this scenario, the resulting electric field is entirely in the axial direction, and so the plasma

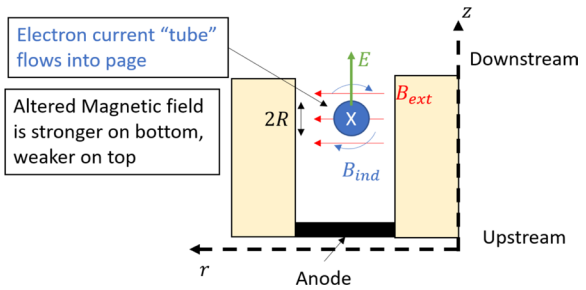

Fig. 4 Sketch of an annular Hall thruster with azimuthal current with induced magnetic field

current forms in the ExB direction. The ExB plasma current travels azimuthally around the thruster channel in a closed loop, inducing a magnetic field of some magnitude B_{ind}. The induced magnetic field vectors and the externally applied magnetic field vectors can be added to determine the total magnetic field at any point. The magnitude of the induced magnetic field within the azimuthal current density j_θ and area A can be written, by the Biot-Savart law, as:

$$B_{ind}(z) = \frac{\mu_0 j_\theta A}{2\pi|z|} = \frac{\mu_0 j_\theta \pi |z|^2}{2\pi|z|} = \frac{\mu_0 j_\theta |z|}{2}, \tag{18}$$

where z is the axial distance from the center of the current tube. Note that the absolute value is used here as the axial term is used in substitution of the conventional radial term of the Bio-Savart law. If we consider the center of the current loop to be our axial zero, we can define the outer radius of this current loop to be R. Given the orientation of the magnetic fields shown in Fig. 4, the total magnetic field in the downstream side and the upstream side of the current loop are simply:

$$\begin{aligned} B(z: -R \rightarrow 0) &= B_{ext} + B_{ind}(z), \\ B(z: 0 \rightarrow +R) &= B_{ext} - B_{ind}(z). \end{aligned} \tag{19}$$

At the edges of the current tube $z = \pm R$, the magnitude of the induced magnetic field reaches a maximum and can be defined as $B_{ind}(z = \pm R) = B_{IND}$.

The component of thrust density due to magnetic pressure in Eq. (17) can then be written in terms of B_{IND} and B_{ext}:

$$
\begin{aligned}
\mathcal{T}_1 &= \int_{z_o}^{z_f} e n_e E_{z,1} dz \\
&= -\int_{z_o}^{z_f} \left(\frac{\vec{\nabla}_\perp (B^2)}{2\mu_0} - \frac{B^2}{\mu_0} \frac{\hat{R}_B}{R_B} \right)_z dz \\
&= -\int_{B(-R)}^{B(R)} \frac{d(B^2)}{2\mu_0} - \int_{z_o}^{z_f} \left(\frac{B^2}{\mu_0} \frac{1}{R_B} \right) dz \\
&= \frac{1}{2\mu_0} \left((B_{ext} + B_{IND})^2 - (B_{ext} - B_{IND})^2 \right) - \int_{z_o}^{z_f} \left(\frac{B^2}{\mu_0} \frac{1}{R_B} \right) dz \\
&= \frac{1}{2\mu_0} (4 B_{IND} B_{ext}) - \int_{z_o}^{z_f} \left(\frac{B^2}{\mu_0} \frac{1}{R_B} \right) dz \,.
\end{aligned}
\tag{20}
$$

Thus in this formulation of an idealized Hall thruster with a simple current loop, the magnetic pressure term scales with both the applied magnetic field B_{ext} and with the induced magnetic field B_{IND} due to the Hall current. The limits of the thrust density due to magnetic pressure are accordingly tied to the limits of these two quantities.

The magnetic tension term requires significantly more simplification due to the radius of curvature term. The radius of curvature R_B of the total magnetic field can be written as a function of both the magnitude and radius of curvature of the external and induced fields, which is derived in Appendix B. It is noted that the radius of curvature of the induced field is simply the distance from the center of the current tube ($R_{B,ind} = z <= R$) and that the radius of curvature of the externally applied field in our ideal model is much larger than the radius of the electron current and correspondingly the radius of curvature of the induced field ($R_{ext} >> R$). A generalized form of thrust density due to magnetic curvature without the latter assumption is found in Appendix B. This curvature will be slightly different for the top of the current tube as compared to the bottom, given the induced fields are opposing the applied field on the top and in the same direction on the bottom:

$$
\frac{1}{R_{top}} = \frac{\frac{B_{ext}^2}{R_{B,ext}} + \frac{B_{ind}^2}{R_{B,ind}} - B_{ind} B_{ext} \left(\frac{1}{R_{B,ind}} \right)}{(B_{ext} - B_{ind})^2} \,, \tag{21}
$$

$$
\frac{1}{R_{bot}} = \frac{\frac{B_{ext}^2}{R_{B,ext}} + \frac{B_{ind}^2}{R_{B,ind}} + B_{ind} B_{ext} \left(\frac{1}{R_{B,ind}} \right)}{(B_{ext} + B_{ind})^2} \,. \tag{22}
$$

We can substitute the radii of curvature of Eq. (21) and Eq. (22) into Eq. (20) to integrate the magnetic tension term over the radius of the current tube R, noting that the orientation of the radius of curvature is negative from z_0 to 0 and positive from 0 to z_f (Fig. 4) and the radius of curvature of the induced field is simply the distance from the center of the current tube z:

$$\begin{aligned}\mathcal{T}_1 &= \frac{4B_{IND}B_{ext}}{2\mu_0} + \int_0^R \left(\frac{(B_{ext}+B_{ind})^2}{\mu_0 R_B}\right)dz - \int_0^R \left(\frac{(B_{ext}-B_{ind})^2}{\mu_0 R_B}\right)dz \\ &= \frac{4B_{IND}B_{ext}}{2\mu_0} + \frac{2}{\mu_0}\int_0^R \left(B_{ind}B_{ext}\left(\frac{1}{z}\right)\right)dz \\ &= \frac{4B_{IND}B_{ext}}{2\mu_0} + \frac{2}{\mu_0}\int_0^R \left(\frac{\mu_0 jz}{2}B_{ext}\left(\frac{1}{z}\right)\right)dz \\ &= \frac{4B_{IND}B_{ext}}{2\mu_0} + \frac{4B_{IND}B_{ext}}{2\mu_0}\,.\end{aligned} \tag{23}$$

Axial plasma resistivity

The second component is related to the plasma resistivity for the axial electron current.

$$E_{z,2} = \frac{m_e \nu}{e^2 n_e} j_z\,, \tag{24}$$

$$\mathcal{T}_2 = \int_{z_o}^{z_f} e n_e E_{z,2} dz = \frac{m_e}{e}\int_{z_o}^{z_f} \nu j_z dz\,. \tag{25}$$

The collision frequency for electrons is typically dominated by the anomalous collision frequency, followed by electron-neutral, electron-wall collisions, and the electron-ion collisions [16, 17]. The electron-neutral collision frequency is typically an order of magnitude above that of the electron-ion collisions, despite the lower neutral density in the acceleration region, due to the relatively high value of the electron temperature (typically $T_e > 20eV$). Utilizing a thruster in this manner is highly inefficient due to the energy losses to the neutrals, however it does represent some contribution to the thrust density. Thrust due to this plasma resistivity may also became appreciable in poor vacuum conditions as the neutral density increases. Higher thrust has been observed in Hall thrusters with higher neutral background density [18], however this may also be due to charge-exchange collisions. It should be noted that as plasma density increases, the electron-ion and ion-neutral collisions become appreciable. These are of particular importance to the operation of MPD thrusters, and while this effect is not investigated here, future work may analyze the thruster operation of a Hall thruster-MPDT hybrid, which may occur at high thrust densities as was explored in recent work [5, 13].

Thus, the total thrust density due to the magnetic field is the sum of the magnetic pressure and the magnetic tension, which have equivalent magnitudes for the idealized annular HET. Essentially, the total magnetic field increases on the upstream side of the current tube and decreases on the downstream side, which creates an axially positive magnetic pressure. The current also induces a curl in the local magnetic field, and the magnetic tension creates a pressure pointing towards the center of the current to straighten this magnetic field. Given that the tension scales by the square of the magnetic field and the magnetic field is higher on the upstream side than the downstream, the net tension points in the positive axial direction and also contributes to thrust. Note that the relative scaling between the magnetic pressure and curvature terms change with the geometry of the magnetic field.

Plasma pressure

The third component due to plasma pressure is:

$$E_{z,3} = -\frac{1}{en_e}\left(\nabla_z(P_\parallel \cos^2\alpha + P_\perp \sin^2\alpha)\right), \tag{26}$$

where it should be noted that when the electron energy is isotropic such that $P_\parallel = P_\perp$, this term reduces to the more familiar form:

$$E_{z,3} = -\frac{1}{en_e}\frac{dP}{dz}. \tag{27}$$

The integral for plasma pressure thrust density is dependent on the angle of the magnetic field over the axial span when considering the anisotropic case, and so for a simplified case of isotropic electron energy, this thrust density component can be derived to be:

$$\mathcal{T}_3 = \int_{z_o}^{z_f} en_e E_{z,3} dz = -\int_{P_{max}}^{0} dP = P_{max}, \tag{28}$$

where the minimum plasma pressure is assumed to be zero, as the thruster is operating in vacuum.

Magnetic mirror

The fourth component is the pressure to the magnetic mirror, which arises when a strong anisotropic electron energy is present in the plasma:

$$E_{z,4} = -\frac{\cos^2\alpha}{en_e}\left(\frac{P_\perp - P_\parallel}{B}\right)\nabla_z B. \tag{29}$$

Much like the plasma pressure term, this is dependent on the angle of the magnetic field, and in general will primarily exist in the center of thrusters where the magnetic field is primarily axial and diverging. Wall-less Hall thrusters and cylindrical Hall thrusters have such conditions, however the anisotropy of the electron energy in the central region is under-investigated. If we assume the angle of the magnetic field over the axial path is relatively constant, as well as that the plasma pressure does not change over the integration path, the thrust density can be derived to be:

$$\begin{aligned}\mathcal{T}_4 &= \int_{z_o}^{z_f} en_e E_{z,4} dz \\ &= -\int_{B_{IND}}^{B_{min}} \cos^2\alpha\left(\frac{P_\perp - P_\parallel}{B}\right) dB \\ &= \cos^2\alpha\left(P_\perp - P_\parallel\right)\ln\left(\frac{B_{max}}{B_{min}}\right).\end{aligned} \tag{30}$$

This is quite similar in form to the thrust derived in Ref. [11] for magnetic nozzle thrusters, however in that case the plasma pressure was assumed to be isotropic.

Table 1 Assumptions of the thrust density magnitudes

Element	Value
n_e	$5 \cdot 10^{17}\,\mathrm{m}^3$
T_e	30 eV
j_z	$0.04\,\mathrm{A/cm}^2$
ν_{en}	10^7 Hz
$z_f - z_0$	0.5 cm
V_D	250 V

Table 2 Relative magnitude of thrust density components

Term	Element	Value
Magnetic Pressure	$\mathcal{T}_1$	$\sim 20\,\mathrm{N/m}^2$
Plasma Resistivity	$\mathcal{T}_2$	$\sim 0.001\,\mathrm{N/m}^2$
Plasma Pressure	$\mathcal{T}_3$	$\sim 2.4\,\mathrm{N/m}^2$
Magnetic Mirror	$\mathcal{T}_4$	$\sim 0\,\mathrm{N/m}^2$
Total	$\mathcal{T}$	$\sim 22\,\mathrm{N/m}^2$

Relative contributions

The relative magnitude of each of the four components of thrust density derived for HET can be estimated using typical operating conditions using the assumptions in Table 1, which were obtained from experimental measurements in a 2 kW HET [19]. The magnetic mirror term was assumed to be zero given the radially dominant fields ($\alpha \sim 0$) and due to the absence of electron temperature anisotropy measurements.

While the value of the thrust density due to axial resistivity, plasma pressure, and the mirror force are relatively straightforward, the magnetic pressure term requires some knowledge of the induced magnetic field, which is not inherently obvious. However an estimate of this induced field can be derived from the applied voltage and the plasma density by the following:

$$j_\theta = \frac{en_eE}{B_{ext}} = \frac{en_e}{B_{ext}}\frac{V_D}{2R}\,, \tag{31}$$

$$B_{IND} = \frac{\mu_0 j_\theta R}{2} = \frac{\mu_0 R}{2}\frac{en_e}{B_{ext}}\frac{V_D}{2R} = \frac{en_e\mu_0 V_D}{4B_{ext}}\,. \tag{32}$$

Here we have assumed the potential drop occurs along the length of the electron tube of diameter $2R$. By substituting B_{IND} into Eq. (23), one can simplify the expression to determine the estimated value of the magnetic pressure and tension thrust density given operating parameters:

$$\mathcal{T}_1 = en_eV_D\,, \tag{33}$$

The values of thrust density for each component is tabulated in Table 2 given the typical operating condition in Table 1, where one may observe that the Magnetic pressure term dominates conventional operation.

Given the simple estimation of Eq. 32, it may appear that the thrust density is only dependent on the applied voltage and is not related to the either the external or induced magnetic field. This is not the case, as the accelerating electric field ultimately is due to the axial reduction of electron mobility due to the magnetic field. The role of B_{ext} in the thrust generation is then to maintain this electron confinement. B_{ind} on the other hand, is a proxy for the plasma density in this confined region, and both directly scale with the thrust density as there are more ions to accelerate, but this higher plasma density also decreases the total magnetic field until confinement no longer occurs. B_{ext} is limited by the magnetic circuit of the thruster. The high magnetic permeability materials of modern thrusters typically saturate with applied magnetic fields of around 20 kG. Given the drop in magnetic flux through the air gap of the discharge channel, the resulting B_{ext} along the channel centerline is typically below 1 kG. Note however, there are alternate designs being investigated such as the air-core magnetic circuit HET, which does not use any magnetically permeable material and may be able to achieve much higher magnetic fields [20]. B_{ind} is largely correlated with the mass flow through the thruster, as the plasma density scales with the mass flow. Limitations on increasing the plasma density and induced field are usually due to thermal management in Hall thrusters, as the heat from the electrons colliding with the channel wall flows to the magnetic circuit and thruster coils/permanent magnet, the latter of which typically have maximum temperatures of $\sim 400°C$. This appears to be the most likely area for future improvements in thrust density, as better thermal designs may allow much higher mass flows and higher thrust densities accordingly.

Role of plume divergence

It should be noted that the thrust density is dependent on the axial component of the electric field, as the radial terms sum to zero due to the axial symmetry of these devices. The radial component of the electric field is ultimately a loss mechanism, as energy is invested into radial acceleration of ions that does not contribute to thrust. The divergence of the plume, which is commonly referred to by an angle at which some fraction of the ion population is accelerated, is a measure of the thrust which is lost. If the plume divergence is defined by the momentum weighted angle at which 50% of ions are accelerated (θ_{mom}), and we assume the ion velocity is not dependent on the acceleration angle, we can define the proportion of thrust density lost to plume divergence. This would be:

$$\cos\left(\theta_{mom}\right) = \frac{2\pi \int_0^{\pi/2} j_i \sin\theta \cos\theta d\theta}{2\pi \int_0^{\pi/2} j_i \sin\theta d\theta}, \tag{34}$$

$$\mathcal{T}_{divergence} = \cos\left(\theta_{mom}\right)\mathcal{T}_{ideal}. \tag{35}$$

Where j_i is the ion current, θ is the plume angle, $\mathcal{T}_{ideal}$ is the ideal thrust density assuming no divergence, and $\mathcal{T}_{divergence}$ is the thrust density taking into account this divergence. This factor directly lowers the thrust density of the thruster (Fig. 5), and

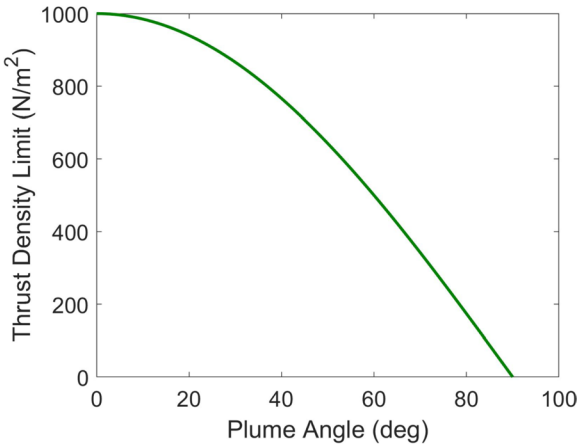

Fig. 5 Example of the thrust density limit as a function of momentum-weighted plume angle. Note that most Hall thrusters operate with a plume angle of about 30 degrees

typically lowers the thrust density to about 85% of the total value for annular Hall thrusters.

Thrust density limit

In general, $\mathcal{T}_1$ is by far the largest component of the thrust density (see Relative contributions section), and the limit of the magnetic pressure/tension component of thrust density can be calculated by considering the limits of the applied and induced magnetic field in the system. The applied field is limited by the saturation of the magnetic field in the high-permeability material of the magnetic circuit. While this is dependent on the actual geometry of the magnetic circuit, a rough estimate using commonly low-carbon steel provides a limit of $B_{ext} = 1$ kG in Hall thruster channels. As the induced field increases, it nullifies the externally applied field in the downstream portion of the current tube. This will reduce the axial confinement of the electrons and eventually transition the operation to that of an MPD thruster rather than a HET due to the induced azimuthal magnetic fields. This hybrid configuration due to higher mass flow and plasma density has been explored recently in Ref. [5, 13]. For a Hall thruster, the current is primarily in the azimuthal direction which is possible due to the much larger electron gyrofrequency ω_{ce} compared to electron cross-field collision frequency ν, the ratio of which is often called the Hall parameter Ω_H. The minimum value of this Hall parameter $\Omega_{H,min}$ is dependent on the geometry of the thruster, and is derived in Appendix C.

$$\Omega_H = \frac{\omega_{ce}}{\nu} > \Omega_{H,min}\,, \tag{36}$$

$$\omega_{ce} = \frac{eB}{m_e}\,. \tag{37}$$

The collision frequency of electrons is the sum of electron-neutral collision frequency (ν_{en}) and an anomalous collision frequency (ν_{anom}). The electron neutral collision frequency is the product of the neutral density and the collision rate,

which is electron temperature dependent ($K(T_e)$) [6]). The neutral density in the acceleration region is typically only about 10% of the plasma density as most of the propellant is ionized in the ionization region. Note that even when n_n is less than 10% of n_e, the electron-ion collision frequency is still much lower than the electron-neutral collision frequency, and so it will be neglected. To keep the collision frequency expression in terms of the plasma density, an effective collision rate will be applied, where $K_{eff} = \frac{n_n}{n_e} K(T_e)$, and is on the order of $1 \cdot 10^{-12}$ m^3/s:

$$\nu = \nu_{en} + \nu_{anom} = n_e K_{eff} + \nu_{anom} \,. \tag{38}$$

The anomalous collision frequency is ascribed to a variety of factors, such as turbulent plasma fluctuations, and electron-wall collisions [21]. Recent work has suggested that the commonly-held assumption that the anomalous electron collision frequency scales by $1/B$ (Bohm-like diffusion) may not be the case in the acceleration region of Hall thrusters [16]. To fully determine the thrust density limit we require some model of how ν_{anom} changes as the thruster is operated at higher power densities, however there is no widely accepted model of electron transport. Instead of deriving it for a single model, the thrust density limit will be derived for 4 separate models of electron transport. As further experimental work at these high thrust densities comes out, we may eventually determine which one of these approaches is correct. The four models that will be analyzed are: 1) assume the anomalous electron frequency does not scale with plasma density, 2) Bohm diffusion, 3) assume the anomalous collision frequency in form of Chodura resistivity, which is a model of electron transport that arises from computer simulations of anomalous transport due to the instabilities of the streaming type [22, 23], and 4) assume the anomalous electron collision frequency scales linearly with the plasma density, which is a worst-case scenario bounding case.

If we use the inequality in Eq. (36) and take into account the induced magnetic field, we can find a limit on the induced field and consequently a limit on the thrust density. The maximum induced field a Hall thruster can support without losing confinement of electrons, and while retaining Hall-thruster operation, can be written as:

$$B_{IND} < B_{ext} - \frac{\Omega_{H,min}(\nu_{en} + \nu_{anom}) m_e}{e} \,. \tag{39}$$

This induced field in Eq. 39 can then be substituted into Eq. 23 to find the thrust density limit in terms of this anomalous collision frequency.

$$\mathcal{T} < \frac{4}{\mu_0} B_{ext}^2 \left(1 - \frac{\Omega_{H,min} m_e (\nu_{en} + \nu_{anom})}{e B_{ext}} \right) . \tag{40}$$

Given that the anomalous collision frequency in some models scales in some way with the plasma density, such as in Chodura resistivity [22], the plasma density is solved by equating the left side of Eq. 40 with Eq. 33:

$$\frac{en_eV_D}{4B_{ext}^2/\mu_0} - 1 < -\frac{\Omega_{H,min}m_e(\nu_{en}+\nu_{anom})}{eB_{ext}}. \tag{41}$$

For all approaches, Eq. 41 is solved for the maximum plasma density, which allows the corresponding maximum thrust density to be solved by substituting that into Eq. 33.

Constant anomalous collision frequency

Given that there is no direct evidence that the anomalous electron transport scales with the plasma density in Hall thrusters, a bounding case can be found where the anomalous electron collision frequency is treated as a constant. This makes the derivation for thrust density relatively simple:

$$\mathcal{T}_{constant} < \frac{4}{\mu_0}B_{ext}^2 \frac{\left(1+\frac{\Omega_{H,min}m_e(\nu_{anom})}{eB_{ext}}\right)}{1+\frac{4B_{ext}^2}{\mu_0}\frac{\Omega_{H,min}m_e}{eB_{ext}}\frac{K_{eff}}{eV_D}}. \tag{42}$$

Modeling of the anomalous electron collision frequency provides values of $\nu_{anom} \sim 10^7$ Hz [16, 17]. This limit is plotted against magnetic field in Fig. 6 alongside the other thrust density limits. The assumption that the anomalous collision frequency remains constant means that the thrust density is essentially limited by the electron-neutral collisions, which start approaching the magnitude of the anomalous collision frequency at these thrust density limits. The high mass flows required to reach this point means that this provides the largest values for the limit compared to the other models, which show more transport at these densities. For $\Omega_{H,min} = 72$ and $\nu_{anom} = 10^7$ Hz, this results in a corresponding thrust density of 1796 N/m^2 at $B_{ext} = 300$ G. At magnetic fields on the order of 300 G, the numerator of the above expression is close to unity, and the expression can be somewhat simplified to:

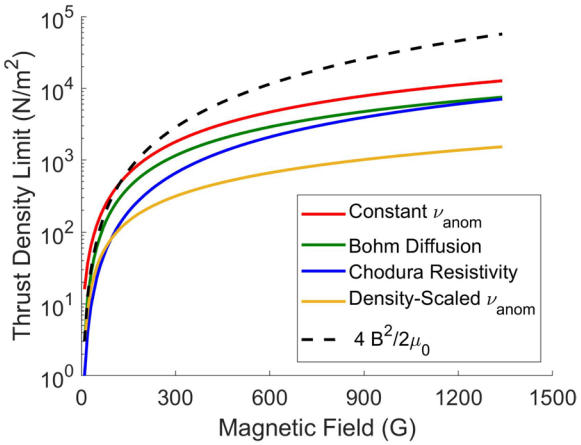

Fig. 6 Calculated thrust density limit versus applied magnetic field for a Hall thruster operating on Xenon with $V_D = 300$ V, minimum Hall parameter = 72, and effective collision rate $K_{eff} = 10^{-12}$ m^3/s, for 5 cases: 1) constant anomalous electron collision frequency where $\nu_{anom} = 10^7$ Hz, 2) Linear scaling of anomalous electron collision frequency where $K_{tot} = 10^{-11}$ m^3/s, 3) Bohm diffusion where $K_B = 0.1$, 4) Chodura resistivity where $C_c = 0.1$, and total magnetic pressure: $4B^2/\mu_0$

$$\mathcal{T}_{constant} < \frac{4}{\mu_0} B_{ext}^2 \frac{1}{1 + \frac{4B_{ext}^2}{\mu_0} \frac{\Omega_{H,min} m_e}{eB_{ext}} \frac{K_{eff}}{eV_D}} . \tag{43}$$

Bohm diffusion

We will now consider the case if the electron transport does follow Bohm-like diffusion and scales by some Bohm constant κ_B and the electron gyrofrequency, which is a form often used in empirical studies of Hall thrusters. The maximum thrust density can be derived in the same way, with the electron-neutral collision frequency scaling by the plasma density and a scaling factor:

$$\nu = \nu_{en} + \nu_{anom} = n_e K_{eff} + \frac{\kappa_B \omega_{ce}}{16} . \tag{44}$$

$$\mathcal{T}_{Bohm} < \frac{4}{\mu_0} B_{ext}^2 \frac{1}{1 + \frac{4B_{ext}^2}{\mu_0} \frac{\Omega_{H,min} m_e}{eB_{ext}} \frac{K_{eff}}{eV_D} \frac{1}{\left(1 - \frac{\kappa_B \Omega_{H,min}}{16}\right)}} . \tag{45}$$

The value of κ_B has been experimentally shown to be below 0.1 in annular HET plasmas [21], however has shown to be higher in other thruster types such as cylindrical Hall thrusters [24]. The induced magnetic field must be smaller than the externally applied magnetic field by a factor that scales with the Bohm diffusion. For $\Omega_{H,min} \sim 72$ and $\kappa_B \sim 0.1$, this results in a thrust density of 1156 N/m^2 at $B_{ext} = 300$ G. This limit over magnetic field can be found in Fig. 6.

Chodura resistivity

An empirical Chodura resistivity [22, 23] was suggested based on the analysis of anomalous transport in computer simulations of the current driven turbulence such as ion-sound, two-stream, and lower hybrid instabilities [25]. As far as the authors are aware, this model of electron transport has not been applied to Hall thruster plasmas. In this model the anomalous electron collision frequency term (ν_{ch}) is written as:

$$\nu_{anom} = \nu_{ch} = C_c \omega_{pi} \left(1 - e^{-\frac{\nu_d}{f v_s}}\right) , \tag{46}$$

where C_c is a scaling factor typically found to be between 0.1 - 1 [22, 23], ω_{pi} is the ion plasma frequency, ν_d is the electron drift velocity, f is another scaling factor which is usually ~ 1, and v_s is the ion sound speed. In the acceleration region $\nu_d >> v_s$, and so this term can be simplified down to:

$$\nu_{ch} \sim C_c \omega_{pi} . \tag{47}$$

For plasma densities on the order of 10^{18} m^{-3}, the chodura frequency roughly matches that of the anomalous collision frequency when $C_c = 0.1$ [16, 17]. Given that the ion plasma frequency contains the square root of the plasma density, the derivation for this term is somewhat more involved, and comes out to:

$$\mathcal{T}_{Chodura} < eV_D \frac{X + Y + Y^2Z/2 - \sqrt{Y^2Z(Y^2Z/4 + X + Y)}}{(X+Y)^2}, \tag{48}$$

where $X = \frac{eV_D}{4B_{ext}^2/\mu_0}$, $Y = \frac{\Omega_{H,min} m_e K_{eff}}{eB_{ext}}$, and $Z = \frac{C_c^2 e^2}{m_i \epsilon_0 K_{eff}^2}$. Given that this model is relatively understudied in Hall thrusters, it is unclear whether it is applicable, however it does appear to provide a thrust density limit in between that of the Bohm model and the linear model (Fig. 6). For $\Omega_{H,min} \sim 72$ and $C_c = 0.1$, this results in a thrust density of 660 N/m^2 at $B_{ext} = 300$ G.

Linear scaling of anomalous collision frequency with plasma density

If we assume the total electron collision frequency scales with the plasma density, noting that this tends to be dominated by the anomalous collision frequency in the acceleration region [16, 17], we can combine the collision rate terms for the anomalous and electron-neutral collision into one term with a single collision rate:

$$K_{eff} n_e + \nu_{anom} = K_{tot} n_e . \tag{49}$$

The thrust density can be derived in a similar fashion as above:

$$\mathcal{T}_{linear} < \frac{4}{\mu_0} B_{ext}^2 \frac{1}{1 + \frac{4B_{ext}^2}{\mu_0} \frac{\Omega_{H,min} m_e}{eB_{ext}} \frac{K_{tot}}{eV_D}} . \tag{50}$$

Given data for Hall thrusters at conventional thrust densities, the effective total collision rate is taken be be 10^{-11} m^3/s [16, 17]. The thrust density for this linear anomalous collision frequency model is also plotted in Fig. 6, which provides the lowest limits of all the models due to the strong dependence on the plasma density. For $\Omega_{H,min} = 72$ and $K_{tot} = 10^{-11}$ m^3/s, this results in a corresponding thrust density of 314 N/m^2 at $B_{ext} = 300$ G. Note that this expression can also be simplified, given that the right side of the denominator is typically much larger than 1:

$$\mathcal{T}_{linear} < \frac{e^2 B_{ext} V_D}{K_{tot} \Omega_{H,min} m_e} . \tag{51}$$

Note that as of revising this article [26] the first published work on a Hall thruster operating at very high power densities was released by Su et al, where a H9 Hall thruster was operated at 10x the power density of standard operation with the use of water cooling to maintain the temperature [27]. The highest achieved thrust density during this ultra high current density operation was 65 N/m^2 (as defined by thruster area, whereas the thrust density defined by the channel area is 122 N/m^2), which appeared at a discharge voltage of 300 V and applied magnetic fields of about 300 G. Note that this is still below the theoretical limits outlined in this paper (314 N/m^2 assuming the conservative linear dependence of anomalous electron collision frequency and plasma density, and 1796 N/m^2 assuming constant anomalous electron collision frequency). This operation provided some insight into what occurs to electron transport at these very high thrust densities: when the power density scaled by a factor of ten there appeared to be minimal difference in the current utilization, suggesting the electron transport does

not significantly change as the plasma density increases. This suggests that approach 1 (no scaling with density) may hold at high power densities, which also provides the highest thrust density limit.

Conclusion

The formulation of thrust density provides some insight into the potential limits of Hall thruster operation. In general, the magnetic pressure and tension term provides the majority of thrust density in annular Hall thrusters, however the magnetic mirror term may provide appreciable magnitudes for thrusters with diverging magnetic fields as shown in recent experiments [14]. The plasma resistivity and pressure terms, while important to the operation of the thruster itself, provide relatively negligible thrust. The limits of thrust density show magnitudes well above that calculated by the conventional operation as defined in Table 1.

If we compare the calculated thrust density with the derived expressions in Table 2 to the measured thrust density in many Hall thrusters, as shown in Fig. 1, a clear linear trend is apparent between measured thrust density and power. This is curious given that this trend occurs over all forms of electric propulsion, despite the vastly different acceleration mechanisms. Hall thrusters appear an outlier in this regard, as rather than following this trend they tend to operate with relatively constant thrust densities of ~ 10 N/m^2 over a large range of power levels. Given that this is several orders of magnitude below their potential thrust density limit of $\sim 10^3$ N/m^2, there appears to be great potential for improvement of these devices through miniaturization or increasing throughput of conventional sized devices.

It is notable that, with the exception of the recent experiment with an H9 Hall thruster, which was still as much as 10x below the theoretical limit [27], no HET has been operated at such higher thrust densities as of writing this article, largely due to material limitations, and the behavior of the plasma and the role of instabilities at these levels is not well understood. These instabilities have not hampered Hall thruster operation yet, however given the relation between the anomalous collision frequency and the maximum thrust density in Fig. 6, minimizing the anomalous collision frequency of electrons may soon be a critical challenge to operating at higher thrust density levels. The path forward appears to be one part an improvement in the engineering of the devices and another part an improvement in the understanding of the physics. The heat management of the devices needs to significantly improve to maintain the magnetic circuit at these high plasma densities, and the anomalous electron transport in the plasma needs to be reduced, likely by suppression of the plasma instabilities. Yet, despite the potential challenges that these may represent, it is clear we are operating these thrusters well below their potential capability.

Appendix A Compiled list of thrust densities

Thrust density for the thrusters in Fig. 1 is defined as the measured thrust in literature divided by the total front-facing area, as compiled in Table 3.

Table 3 Compiled list of thrust densities and power levels of several forms of electric propulsion in descending order of measured thrust density

MPD Thruster	Organization	Thrust Density (N/m^2)	Power (kW)	Reference
MY-III	Osaka University	14,012	3,630	[28]
MultiMegawatt MPDT	Princeton University	10,186	2,800	[29]
X-2 Alkali	AVCO-RAD	944	123	[28]
LAJ-AF-2	EOS	759	21	[28]
130 kW Lithium MPDT	RIAME MAI	145	130	[30]
X16	Stuttgart/DFVLR	120	15	[28]
Li LFA	Princeton University	116	100	[31]
Tokyo10kW	Tokyo University	32	7	[28]
Hall Thruster	Organization	Thrust Density (N/m^2)	Power (kW)	Reference
SPT-290	Fakel	22.7	30	[32]
BHT-8000	Busek	22.3	8	[33]
SPT-140	Fakel	18.6	4.6	[34]
NASA-400M	NASA	16.7	47	[35]
NASA-300M	NASA	16.0	20	[36]
SPT-200	Fakel	15.8	11	[32]
BHT-20k	Busek	14.1	20	[37]
NASA-457Mv2	NASA	14.0	50	[38]
T-220	NASA	13.2	10	[39]
PPS-20k	Snecma	13.1	23.5	[40]
PPS-1350	Snecma	12.7	1.8	[41]
BHT-600	Busek	12.1	0.8	[42]
SPT-100	Fakel	11.5	1.4	[43]
CHTpm	PPPL	10.6	0.18	[44]
BHT-1500	Busek	9.1	1.8	[45]
Ion Thruster	Organization	Thrust Density (N/m^2)	Power (W)	Reference
XIPS 25cm	L3 Technologies	3.4	4.3	[6]
NEXT	NASA	2.3	6.9	[46]
T5 Kaufman	Mitsubishi	2.3	0.5	[6]
ETS-8 Kaufman	Mitsubishi	2.1	0.6	[6]
RIT-RD	Astrium	1.9	0.5	[6]
NSTAR	NASA	1.3	2.3	[47]
XIPS 10cm	L3 Technologies	1.3	0.4	[6]
μ10 ECR	JAXA	0.1	0.3	[6]
Electrospray Thruster	Organization	Thrust Density (N/m^2)	Power (W)	Reference
Indium MEP 2016	JPL	0.29	3.5	[48]
BET-1mN	Busek	0.097	15	[49]
S-iEPS thruster	NASA/MIT	0.06	0.15	[50]
TILE	NASA/MIT	0.058	10	[50]
TILE 3	Accion	0.045	20	[51]
BET-100	Busek	0.012	5.5	[52]

Appendix B Magnetic Curvature

The radius of curvature for a given field falls out of the tension term of a field line:

$$(\vec{B}\cdot\vec{\nabla})\vec{B} = B\frac{d(B\hat{s})}{ds} = B^2\frac{d(\hat{s})}{ds} + B\frac{dB}{ds}\hat{s} = B^2\frac{\hat{n}}{R_B} + \hat{s}\frac{d(B^2)}{2ds}. \tag{52}$$

The radius of curvature can then be written, in the common inverse form, as the amplitude of the normal component $\hat{n}$:

$$\frac{1}{R_B} = \frac{\left\|(\vec{B}\cdot\vec{\nabla})\vec{B} - \hat{s}\frac{d(B^2)}{2ds}\right\|}{\vec{B}\cdot\vec{B}}. \tag{53}$$

To determine the total radius of curvature for the superposition of two fields, such as the induced magnetic field and the existing external field, we can express the total magnetic field as the sum of these two fields: $\vec{B} = \vec{B}_{ind} + \vec{B}_{ext}$.

$$\begin{aligned}\frac{1}{R_B} &= \frac{\left\|((\vec{B}_{ext}+\vec{B}_{ind})\cdot\vec{\nabla})(\vec{B}_{ext}+\vec{B}_{ind}) - \hat{s}\frac{d(B^2)}{2ds}\right\|}{(\vec{B}_{ext}+\vec{B}_{ind})\cdot(\vec{B}_{ext}+\vec{B}_{ind})} \\ &= \frac{\left\|(\vec{B}_{ind}\cdot\vec{\nabla})\vec{B}_{ind} + (\vec{B}_{ind}\cdot\vec{\nabla})\vec{B}_{ext} + (\vec{B}_{ext}\cdot\vec{\nabla})\vec{B}_{ind} + (\vec{B}_{ext}\cdot\vec{\nabla})\vec{B}_{ext} - \hat{s}\frac{d(B^2)}{2ds}\right\|}{(\vec{B}_{ext}+\vec{B}_{ind})\cdot(\vec{B}_{ext}+\vec{B}_{ind})}.\end{aligned} \tag{54}$$

The final term on the right hand side can be expanded to:

$$\begin{aligned}-\hat{s}\frac{d(B^2)}{2ds} &= -\hat{s}\frac{d((\vec{B}_{ext}+\vec{B}_{ind})\cdot(\vec{B}_{ext}+\vec{B}_{ind}))}{2ds} \\ &= -\hat{s}\frac{d(B_{ind}^2 + B_{ext}^2 + 2\vec{B}_{ext}\cdot\vec{B}_{ind})}{2ds}.\end{aligned} \tag{55}$$

The radius of curvature for the induced and external fields can be substituted into Eq. (55) to simplify, where it is noted that along the integration path $\vec{B}_{ind}$ and $\vec{B}_{ext}$ are parallel and the radii of curvature vector for the induced and external field are in the same direction:

$$\begin{aligned}\frac{1}{R_B} &= \left\|\left((\vec{B}_{ind}\cdot\vec{\nabla})\vec{B}_{ind} - \hat{s}\frac{d(B_{ind}^2)}{2ds}\right) + \left((\vec{B}_{ext}\cdot\vec{\nabla})\vec{B}_{ext} - \hat{s}\frac{d(B_{ext}^2)}{2ds}\right)\right. \\ &\quad + (\vec{B}_{ind}\cdot\vec{\nabla})\vec{B}_{ext} + (\vec{B}_{ext}\cdot\vec{\nabla})\vec{B}_{ind} \\ &\quad \left. - \hat{s}\frac{d(2\vec{B}_{ext}\cdot\vec{B}_{ind})}{2ds}\right\| \Big/ \left((\vec{B}_{ext}+\vec{B}_{ind})\cdot(\vec{B}_{ext}+\vec{B}_{ind})\right) \\ &= \frac{\left\|\frac{\hat{n}B_{ind}^2}{R_{B,ind}} + \frac{\hat{n}B_{ext}^2}{R_{B,ext}} + (\vec{B}_{ind}\cdot\vec{\nabla})\vec{B}_{ext} + (\vec{B}_{ext}\cdot\vec{\nabla})\vec{B}_{ind} - \hat{s}\frac{d(\vec{B}_{ext}\cdot\vec{B}_{ind})}{ds}\right\|}{(\vec{B}_{ext}+\vec{B}_{ind})\cdot(\vec{B}_{ext}+\vec{B}_{ind})}.\end{aligned} \tag{56}$$

This equation can be further simplified by finding the change of $\vec{B}_{ext}$ along $\vec{B}_{ind}$, noting that along the integration path $\hat{s}_{ext} = \hat{s} = \pm\hat{s}_{ind}$, where the induced field is in the same direction below the current tube and in the opposite direction above the current tube:

$$
\begin{aligned}
(\vec{B}_{ind} \cdot \vec{\nabla})\vec{B}_{ext} &= B_{ind}\frac{d(B_{ext}\hat{s}_{ext})}{ds_{ind}} \\
&= B_{ind}B_{ext}\frac{d\hat{s}_{ext}}{ds_{ind}} + B_{ind}\hat{s}_{ext}\frac{dB_{ext}}{ds_{ind}} \\
&= (\hat{s}_{ind}\cdot\hat{s}_{ext})\left(B_{ind}B_{ext}\frac{\hat{n}}{R_{B,ext}} + \hat{s}\frac{d(B_{ext}B_{ind})}{ds} - B_{ext}\hat{s}\frac{dB_{ind}}{ds}\right).
\end{aligned} \tag{57}
$$

The change of $\vec{B}_{ind}$ along $\vec{B}_{ext}$ can be found in the same manner, which provides a sum of:

$$
\begin{aligned}
(\vec{B}_{ind} \cdot \vec{\nabla})\vec{B}_{ext} + (\vec{B}_{ext} \cdot \vec{\nabla})\vec{B}_{ind} = (\hat{s}_{ind}\cdot\hat{s}_{ext})\Bigg(B_{ind}B_{ext}\left(\frac{\hat{n}}{R_{B,ext}} + \frac{\hat{n}}{R_{B,ind}}\right) \\
+ \hat{s}\frac{d(B_{ext}B_{ind})}{ds}\Bigg)
\end{aligned} \tag{58}
$$

This can then be substituted into Eq. (56), noting that the radius of curvature is defined by the amplitude of the normal component:

$$
\frac{1}{R_B} = \frac{\frac{B_{ind}^2}{R_{B,ind}} + \frac{B_{ext}^2}{R_{B,ext}} + (\hat{s}_{ind}\cdot\hat{s}_{ext})B_{ind}B_{ext}\left(\frac{1}{R_{B,ext}} + \frac{1}{R_{B,ind}}\right)}{(\vec{B}_{ext} + \vec{B}_{ind})\cdot(\vec{B}_{ext} + B_{ind})}. \tag{59}
$$

The bottom (R_{bot}) and the top (R_{top}) radii of curvature are finally:

$$
\frac{1}{R_{top}} = \frac{\frac{B_{ext}^2}{R_{B,ext}} + \frac{B_{ind}^2}{R_{B,ind}} - B_{ind}B_{ext}\left(\frac{1}{R_{B,ind}} + \frac{1}{R_{B,ext}}\right)}{(B_{ext} - B_{ind})^2}, \tag{60}
$$

$$
\frac{1}{R_{bot}} = \frac{\frac{B_{ext}^2}{R_{B,ext}} + \frac{B_{ind}^2}{R_{B,ind}} + B_{ind}B_{ext}\left(\frac{1}{R_{B,ind}} + \frac{1}{R_{B,ext}}\right)}{(B_{ext} + B_{ind})^2}. \tag{61}
$$

We can substitute the radii of curvature of Eq. (60) and Eq. (61) into Eq. (20) to integrate the magnetic tension term over the radius of the current tube R, noting that the orientation of the radius of curvature is negative from z_0 to 0 and positive from 0 to z_f (Fig. 4) and the radius of curvature of the induced field is simply the distance from the center of the current tube z ($R_{B,ind} = z$):

$$\begin{aligned}
\mathcal{T}_1 &= \frac{4B_{IND}B_{ext}}{2\mu_0} + \int_0^R \left(\frac{(B_{ext}+B_{ind})^2}{\mu_0 R_B}\right)dz - \int_0^R \left(\frac{(B_{ext}-B_{ind})^2}{\mu_0 R_B}\right)dz \\
&= \frac{4B_{IND}B_{ext}}{2\mu_0} + \frac{1}{\mu_0}\int_0^R \left(\frac{B_{ext}^2}{R_{B,ext}} + \frac{B_{ind}^2}{R_{B,ind}} + B_{ind}B_{ext}\left(\frac{1}{R_{B,ind}} + \frac{1}{R_{B,ext}}\right)\right)dz \\
&- \frac{1}{\mu_0}\int_0^R \left(\frac{B_{ext}^2}{R_{B,ext}} + \frac{B_{ind}^2}{R_{B,ind}} - B_{ind}B_{ext}\left(\frac{1}{R_{B,ind}} + \frac{1}{R_{B,ext}}\right)\right)dz \\
&= \frac{4B_{IND}B_{ext}}{2\mu_0} + \frac{2}{\mu_0}\int_0^R \left(B_{ind}B_{ext}\left(\frac{1}{z} + \frac{1}{R_{B,ext}}\right)\right)dz \\
&= \frac{4B_{IND}B_{ext}}{2\mu_0} + \frac{2}{\mu_0}\int_0^R \left(\frac{\mu_0 jz}{2}B_{ext}\left(\frac{1}{z} + \frac{1}{R_{B,ext}}\right)\right)dz \\
&= \frac{4B_{IND}B_{ext}}{2\mu_0} + \frac{4B_{IND}B_{ext}}{2\mu_0}\left(1 + \frac{R}{2R_{B,ext}}\right).
\end{aligned} \tag{62}$$

If we assume the radius of curvature of the externally applied magnetic field is very large compared to the radius of the current tube ($R_{ext} >> R$), which we expect for straight radial magnetic fields and as is shown in the main text, Eq. (62) simplifies to the following:

$$\mathcal{T}_1 \approx \frac{4B_{IND}B_{ext}}{2\mu_0} + \frac{4B_{IND}B_{ext}}{2\mu_0}. \tag{63}$$

However it is noted that a lower radius of curvature on the externally applied field provides an increase to the thrust density by this additional term $\frac{4B_{IND}B_{ext}}{2\mu_0}\frac{R}{2R_{B,ext}}$.

Appendix C Minimum Hall Parameter

The value of the Hall parameter should correspond to the condition where the electrons display closed drift behavior. That is, the electrons complete a rotation around the thruster channel faster than they move through the acceleration region. This can be written in terms of an inequality:

$$\frac{v_\theta}{2\pi R_{chan}} > \frac{v_z}{L_{acc}}, \tag{64}$$

where we have defined the azimuthal electron speed v_θ, the thruster channel radius R_{chan}, the electrons to move axially with speed v_z and the acceleration region length to be L_{acc}. In our idealized model of the Hall thruster where the electrons are focused in a tube of radius R, if we assume the voltage drop is localized in this tube then the length of the acceleration region corresponds to the diameter of the tube; $L_{acc} = 2R$. Noting that the axial electron velocity is due to the drift of electrons by frequency ν and gyroradius r_{Le}:

$$\frac{v_\theta}{2\pi R_{chan}} > \nu\frac{r_{Le}}{2R}, \tag{65}$$

By taking the azimuthal electron velocity to be due to $E \times B$ drift, we can transform this inequality into one with the Hall parameter, where we take the electron velocity in gyromotion to be the thermal electron speed:

$$\begin{aligned} \frac{v_\theta}{2\pi R_{chan}} &> \nu \frac{r_{Le}}{2R}, \\ \frac{E}{2\pi R_{chan} B} &> \nu \frac{v_e m_e}{2ReB}, \\ \frac{V_D/2R}{2\pi R_{chan} B\nu} &> \frac{m_e}{2ReB}\sqrt{\frac{T_e}{m_e}}, \\ \Omega_H &> \frac{2\pi R_{chan} B}{V_D}\sqrt{\frac{T_e}{m_e}}, \end{aligned} \tag{66}$$

For a typical Hall thruster with $T_e = 30eV$, $V_D = 300V$, $B = 300G$, and $R_{chan} = 5cm$, the $\Omega_{H,min} = 72$.

Acknowledgements
The authors would like to thank Nathaniel J Fisch and Amnon Fruchtman for fruitful discussion of thrust density limits of plasma thrusters and for motivating this research. The authors would like to acknowledge Igor Kaganovich and Nirbhav Chopra for fruitful discussions.

Authors' contributions
All authors contributed to the study conception and design. Yevgeny Raitses formulated the objectives of this study. The first draft of the manuscript was written by Jacob Simmonds and all authors commented on previous versions of the manuscript. All authors read and approved the final manuscript.

Funding
This work was supported by the AFOSR under contract FA9550-17-1-0010 and the US Department of Energy under contract DE-AC02-09CH11466.

Availability of data and materials
All data generated or analysed during this study are included in this published article.

Declarations

Competing interests
The authors declare no competing interests.

Received: 13 November 2022 Accepted: 19 March 2023
Published online: 30 March 2023

References

1. Lev D, Myers R, Lemmer K, Kolbeck K, Keidar M, Koizumi H, et al. The Technological and Commercial Expansion of Electric Propulsion in the Past 24 Years. In: Proceedings of the 35th International Electric Propulsion Conference. vol. IEPC-2017-242. Atlanta; 2017
2. Snyder JS, Lenguito G, Frieman JD, Haag TW, Mackey JA (2020) Effects of Background Pressure on SPT-140 Hall Thruster Performance. J Propuls Power. 36(5):668–676. https://doi.org/10.2514/1.B37702
3. Zharinov AV, Popov YS (1967) Acceleration of plasma by a closed Hall current. Sov Phys-Tech Phys. 12:208–211
4. Kim VP (2015) Design features and operating procedures in advanced Morozov's stationary plasma thrusters. Tech Phys. 60(3):362–375. https://doi.org/10.1134/S1063784215030135
5. Sasoh A, Kasuga H, Nakagawa Y, Matsuba T, Ichihara D, Iwakawa A (2018) Electrostatic-magnetic-hybrid thrust generation in central-cathode electrostatic thruster (CC-EST). Acta Astronautica. 152:137–145. https://doi.org/10.1016/j.actaastro.2018.07.052
6. Goebel DM, Katz I. Fundamentals of electric propulsion: ion and Hall thrusters. No. 1 in JPL space science and technology series. Hoboken: Wiley; 2008. OCLC: ocn233939832
7. Peterson P, Gallimore A. The performance and plume characterization of a laboratory gridless ion thruster with closed electron drift acceleration. In: 40th AIAA/ASME/SAE/ASEE Joint Propulsion Conference and Exhibit. Fort Lauderdale: American Institute of Aeronautics and Astronautics; 2004. p. 3936
8. Patterson M. Next-generation electric propulsion thrusters. In: 47th AIAA/ASME/SAE/ASEE Joint Propulsion Conference & Exhibit. San Diego: American Institute of Aeronautics and Astronautics; 2011. p. 5812

9. Smirnov A, Raitses Y, Fisch NJ (2005) Maximizing ion current by space-charge neutralization using negative ions and dust particles. Phys Plasmas. 12(5):053503. https://doi.org/10.1063/1.1897715
10. Raitses Y, Fisch NJ (2001) Parametric investigations of a nonconventional Hall thruster. Phys Plasmas. 8(5):2579–2586. https://doi.org/10.1063/1.1355318
11. Fruchtman A, Takahashi K, Charles C, Boswell RW (2012) A magnetic nozzle calculation of the force on a plasma. Phys Plasmas. 19(3):033507. https://doi.org/10.1063/1.3691650
12. Takahashi K, Lafleur T, Charles C, Alexander P, Boswell RW (2011) Electron Diamagnetic Effect on Axial Force in an Expanding Plasma: Experiments and Theory. Phys Rev Lett. 107:235001. https://doi.org/10.1103/PhysRevLett.107.235001
13. Sasoh A, Mizutani K, Iwakawa A (2017) Electrostatic/magnetic ion acceleration through a slowly diverging magnetic nozzle between a ring anode and an on-axis hollow cathode. AIP Adv. 7(6):065204. https://doi.org/10.1063/1.4985380
14. Simmonds J, Raitses Y (2021) Ion acceleration in a wall-less Hall thruster. J Appl Phys. 130(9):093302. https://doi.org/10.1063/5.0062607
15. Comfort RH. The magnetic mirror force in plasma fluid Models. In: Moore TE, Waite JH, Moorehead TW, Hanson WB, editors. Geophysical Monograph Series. vol. 44. Washington, D. C.: American Geophysical Union. 1988. p. 51–53. https://doi.org/10.1029/GM044p0051
16. Mikellides IG, Ortega AL (2019) Challenges in the development and verification of first-principles models in Hall-effect thruster simulations that are based on anomalous resistivity and generalized Ohm's law*. Plasma Sources Sci Technol. 28(1):014003. https://doi.org/10.1088/1361-6595/aae63b
17. Hofer R, Katz I, Goebel D, Jameson K, Sullivan R, Johnson L, et al. Efficacy of Electron Mobility Models in Hybrid-PIC Hall Thruster Simulations. https://doi.org/10.2514/6.2008-4924
18. Fruchtman A (2011) The Thrust of a Collisional-Plasma Source. IEEE Trans Plasma Sci. 39(1):530–539. https://doi.org/10.1109/TPS.2010.2089067
19. Staack D, Raitses Y, Fisch NJ (2004) Shielded electrostatic probe for nonperturbing plasma measurements in Hall thrusters. Rev Sci Instrum. 75(2):393–399. https://doi.org/10.1063/1.1634353
20. Hurley W, Marks TA, Jorns B. Design of an Air-Core Circuit for a Hall Thruster. In: AIAA SCITECH 2023 Forum. https://doi.org/10.2514/6.2023-0841
21. Boeuf JP (2017) Tutorial: Physics and modeling of Hall thrusters. J Appl Phys. 121(1):011101. https://doi.org/10.1063/1.4972269
22. Biskamp D, Chodura R (1971) Computer Simulation of Anomalous dc Resistivity. Phys Rev Lett. 27:1553–1556. https://doi.org/10.1103/PhysRevLett.27.1553
23. Kayama ME (2012) Resistivity in the dynamic current sheath of a field reversed configuration. Phys Plasmas. 19(3):032511. https://doi.org/10.1063/1.3698405
24. Smirnov AN, Raitses Y, Fisch NJ (2006) Electron cross-field transport in a miniaturized cylindrical Hall thruster. IEEE Trans Plasma Sci. 34(2):132–141. https://doi.org/10.1109/TPS.2006.872185
25. Tummel K, Ellison CL, Farmer WA, Hammer JH, Parker JB, LeChien KR (2020) Kinetic simulations of anomalous resistivity in high-temperature current carrying plasmas. Phys Plasmas. 27(9):092306
26. Simmonds J, Raitses Y, Smolyakov A. A Theoretical Thrust Density Limit for Hall Thrusters. 2022. arXiv. https://doi.org/10.48550/ARXIV.2212.01486
27. Su LL, Roberts PJ, Gill T, Hurley W, Marks TA, Sercel CL, et al. Operation and Performance of a Magnetically Shielded Hall Thruster at Ultrahigh Current Densities on Xenon and Krypton. In: AIAA SCITECH 2023 Forum. https://doi.org/10.2514/6.2023-0842
28. Kodys A, Choueiri E. In: A Critical Review of the State-of-the-Art in the Performance of Applied-Field Magnetoplasmadynamic Thrusters. https://doi.org/10.2514/6.2005-4247
29. Burton RL, Clark KE, Jahn RG (1983) Measured performance of a multimegawatt MPD thruster. J Spacecr Rocket. 20(3):299–304. https://doi.org/10.2514/3.25596
30. Tikhonov VB, Semenikhin SA, Brophy JR, Polk JE. Performance of a 130 kW MPD Thruster with an External Magnetic Field and Li as a Propellant. In: Proceedings of the 25th International Electric Propulsion Conference. vol. IEPC-1997-117. Cleveland: Electric Rocket Propulsion Society; 1997.
31. Choueiri E, Chiravalle V, Miller G, Jahn R, Anderson W, Bland J. Lorentz Force Accelerator with an open-ended lithium heat pipe. In: 32nd AIAA/ASME/SAE/ASEE Joint Propulsion Conference. Lake Buena Vista: American Institute of Aeronautics and Astronautics; 1996. AIAA-1996-2737. https://doi.org/10.2514/6.1996-2737
32. Jankovsky R, Tverdokhlebov S, Manzella D. High Power Hall Thrusters. In: Proceedings of the 35th Joint Propulsion Conference. vol. AIAA 99-2949. Los Angeles: Electric Rocket Propulsion Society; 1999.
33. Pote B, Hruby V, Monheiser J. Performance of an 8 kW Hall Thruster. In: Proceedings of the 26th International Electric Propulsion Conference. vol. IEPC-99-080. Kitakyushu: Electric Rocket Propulsion Society; 1999.
34. Manzella D, Sarmiento C, Saknovic J, Haag T. Performance Evaluation of the SPT-140. In: Proceedings of the 25th International Electric propulsion Conference. vol. IEPC-97-059. Cleveland: Electric Rocket Propulsion Society; 1997.
35. Jacobson D, Manzella D, Hofer R, Peterson P. NASA's 2004 Hall Thruster Program. In: Proceedings of the 40th Joint Propulsion Conference. vol. AIAA-2004-3600. Fort Lauderdale: American Institute of Aeronautics and Astronautics; 2004.
36. Kamhawi H, Haag T, Smith T, Herman D, Huang W, Shastry R, et al. Performance Characterization of the Air Force Transformational Satellite 12 kW Hall Thruster. In: Proceedings of the Spacecraft Propulsion Conference. Colorado Springs: Association Aeronautique et Astronautique de France; 2013.
37. Szabo J, Pote B, Hruby V, Byrne L, Tadrake R, Kolencik G, et al. A Commercial One Newton Hall Effect Thruster for High Power In-Space Missions. In: 47th AIAA/ASME/SAE/ASEE Joint Propulsion Conference & Exhibit. San Diego: American Institute of Aeronautics and Astronautics; 2011. https://doi.org/10.2514/6.2011-6152
38. Soulas G, Haag T, Herman D, Huang W. Performance Test Results of the NASA-457M v2 Hall Thruster. In: Proceedings of the 48th Joint Propulsion Conference. vol. AIAA-2012-3940. Atlanta: American Institute of Aeronautics and Astronautics; 2012.
39. Mason L, Jankovsky R, Manzella D. 1000 hours of testing on a 10 kilowatt Hall effect thruster. In: 37th Joint Propulsion Conference and Exhibit. Salt Lake City: American Institute of Aeronautics and Astronautics; 2001. https://doi.org/10.2514/6.2001-3773

40. Zurbach S, Cornu N, Lasgorceix P. Performance Evaluation of a 20 kW Hall Effect Thruster. In: Proceedings of the 32nd International Electric Propulsion Conference. vol. IEPC-2011-020. Wiesbaden: Electric Rocket Propulsion Society; 2011.
41. Albarede L, Bouchoule A, Lazurenko A, Kim V, Kozlov V, Skrylnikov A. Characteristics of PPS-1350 type thrusters under increased discharge voltages and comparison with hybrid codes simulation results. In: Proceedings of the The 29th International Electric Propulsion Conference. vol. IEPC-2005-136. Princeton: Princeton University; 2005
42. Szabo JJ, Byrne L, Strain M, Paintal S, Sawyer S, Yu T, et al. One Million Newton-Second Duration Test of a 600 Watt Hall Effect Thruster Fueled By Xenon. In: AIAA Propulsion and Energy 2020 Forum. VIRTUAL EVENT. American Institute of Aeronautics and Astronautics; 2020. https://doi.org/10.2514/6.2020-3651
43. Sankovic J, Hamley J, Haag T. Performance evaluation of the Russian SPT-100 thruster at NASA LeRC. In: Proceedings of the 23rd International Electric Propulsion Conference. vol. IEPC-93-094. Seattle: Electric Rocket Propulsion Society; 1994.
44. Polzin K, Raitses Y, Gayoso J, Fisch N. Comparisons in Performance of Electromagnet and Permanent-Magnet Cylindrical Hall-Effect Thrusters. In: 46th AIAA/ASME/SAE/ASEE Joint Propulsion Conference & Exhibit. Nashville: American Institute of Aeronautics and Astronautics; 2010. https://doi.org/10.2514/6.2010-6695
45. Diamant K, Curtiss T, Spektor R, Beiting E, Hruby V, Pote B, et al. Performance and Plume Characterization of the BHT-1500 Hall Thruster. In: Proceedings of the 30th International Electric Propulsion Conference. vol. IEPC-2015-69. Kobe-Hyogo; 2015
46. Anderson JR, Goodfellow KD, Polk JE, Rawlin VK, Sovey JS. Performance characteristics of the NSTAR ion thruster during an on-going long duration ground test. 2000 IEEE Aerosp Conf Proc (Cat No00TH8484). 2000;4:99–122
47. Crofton M, Pollard J, Beiting E, Spektor R, Diamant K, Eapen X, et al. In: Characterization of the NASA NEXT Thruster. https://doi.org/10.2514/6.2009-4815
48. Marrese-Reading C. In: Microfluidic Electrospray Propulsion(MEP) Thruster Performance with Microfabricated Emitter Arrays for Indium Propellant. https://doi.org/10.2514/6.2016-4738
49. Busek Space Propulsion and Systems. Busek-1mN Busek Electrospray Thruster. 2019. http://www.busek.com/index_htm_files/7000850020BET-1mN20Data20Sheet20RevH.pdf. Accessed Oct 2021.
50. Krejci D, Lozano P. Scalable ionic liquid electrospray thrusters for nanosatellites. In: Proceedings of the 39th Annual AAS GNC Conference. Breckenridge: American Astronautical Society; 2016.
51. Accion Systems. Tile 3 Datasheet: Technical Specifications. 2020. https://catalog.orbitaltransports.com/content/brands/accion/Accion%20Systems%20TILE%203%20Datasheet_Nov%202020.pdf. Accessed Oct 2021.
52. Propulsion BS, Systems. Busek-100 Busek Electrospray Thruster. 2017. http://www.busek.com/index_htm_files/70008516F.pdf. Accessed Oct 2021.

Publisher's Note